

## Planck early results IX : XMM-Newton follow-up for validation of Planck cluster candidates

Aghanim, N.

2011

---

Aghanim , N , Juvela , M , Keihänen , E , Keskitalo , R T , Kurki-Suonio , H , Poutanen , T J & Planck Collaboration 2011 , ' Planck early results IX : XMM-Newton follow-up for validation of Planck cluster candidates ' , Astronomy & Astrophysics , vol. 536 , pp. A9 . <https://doi.org/10.1051/0004-6361/201116460>

---

<http://hdl.handle.net/10138/233725>

<https://doi.org/10.1051/0004-6361/201116460>

---

other

publishedVersion

---

Downloaded from Helda, University of Helsinki institutional repository.

This is an electronic reprint of the original article.

This reprint may differ from the original in pagination and typographic detail.

Please cite the original version.

# Planck early results. IX. XMM-Newton follow-up for validation of Planck cluster candidates

Planck Collaboration: N. Aghanian<sup>18</sup>, M. Arnaud<sup>69</sup>, M. Ashdown<sup>67,4</sup>, J. Aumont<sup>8</sup>, C. Baccigalupi<sup>70</sup>, A. Balbi<sup>30</sup>, A. J. Banday<sup>78,7,64</sup>, R. B. Barreiro<sup>4</sup>, M. Bartelmann<sup>78,64</sup>, J. G. Bartlett<sup>55</sup>, E. Battane<sup>90</sup>, K. Benabed<sup>9</sup>, A. Benoit<sup>47</sup>, J.-P. Bernard<sup>7</sup>, M. Bersanelli<sup>7,42</sup>, R. Bhatia<sup>5</sup>, J. J. Boc<sup>58</sup>, A. Bonaldi<sup>38</sup>, J. R. Bond<sup>1</sup>, J. Borrill<sup>63,74</sup>, F. R. Bouchet<sup>49</sup>, M. L. Brown<sup>4,57</sup>, M. Bucher<sup>2</sup>, C. Burigana<sup>1</sup>, P. Cabell<sup>20</sup>, C. M. Cantalupo<sup>63</sup>, J.-F. Cardoso<sup>60,3,49</sup>, P. Carvalho<sup>1</sup>, A. Catalano<sup>3,58</sup>, L. Cayón<sup>20</sup>, A. Challinor<sup>51,57,11</sup>, A. Chambaud<sup>5</sup>, L.-Y. Chiang<sup>50</sup>, G. Chon<sup>65,4</sup>, P. R. Christensen<sup>68,31</sup>, E. Churazov<sup>64,73</sup>, D. L. Clements<sup>45</sup>, S. Colafrancesco<sup>38</sup>, S. Colombi<sup>9</sup>, F. Couchot<sup>62</sup>, A. Coulais<sup>58</sup>, B. P. Crill<sup>65,69</sup>, F. Cuttaia<sup>1</sup>, A. Da Silva<sup>10</sup>, H. Dahle<sup>52,9</sup>, L. Danese<sup>20</sup>, P. de Bernardis<sup>26</sup>, G. de Gasperi<sup>38</sup>, A. de Rosá<sup>1</sup>, G. de Zotti<sup>38,70</sup>, J. Delabrouille<sup>1</sup>, J.-M. Delouis<sup>9</sup>, F.-X. Désert<sup>44</sup>, J. M. Diego<sup>64</sup>, K. Dolag<sup>64</sup>, S. Donzel<sup>12,52</sup>, O. Doré<sup>5,8</sup>, U. Dörl<sup>64</sup>, M. Douspis<sup>48</sup>, X. Dupac<sup>25</sup>, G. Efstathiou<sup>1</sup>, T. A. Enßlin<sup>64</sup>, F. Finelli<sup>41</sup>, I. Flores-Cacho<sup>3,32</sup>, O. Forn<sup>79,7</sup>, M. Frailis<sup>40</sup>, E. Franceschi<sup>1</sup>, S. Fromenteau<sup>48</sup>, S. Galeotti<sup>4</sup>, K. Gangui<sup>46</sup>, R. T. Génova-Santos<sup>53,32</sup>, M. Giard<sup>79,7</sup>, G. Giardini<sup>60</sup>, Y. Giraud-Héraud<sup>1</sup>, J. González-Núñez<sup>78</sup>, R. González-Riestra<sup>74</sup>, K. M. Górski<sup>55,82</sup>, S. Gratton<sup>57,51</sup>, A. Gregorio<sup>28</sup>, A. Gruppuso<sup>1</sup>, D. Harrison<sup>51,57</sup>, P. Heinämäki<sup>77</sup>, S. Henrot-Versillat<sup>1</sup>, C. Hernández-Monteagudo<sup>64</sup>, D. Herranz<sup>54</sup>, S. R. Hildebrandt<sup>3,61,53</sup>, E. Hivon<sup>49</sup>, M. Hobson<sup>1</sup>, W. A. Holmes<sup>55</sup>, W. Hovest<sup>64</sup>, R. J. Hoyland<sup>59</sup>, K. M. Hu<sup>59</sup>, M. J. Jarvis<sup>1</sup>, G. Hurier<sup>61</sup>, A. H. J. Jaffe<sup>45</sup>, M. Juvela<sup>9</sup>, E. Keihänen<sup>19</sup>, R. Keskitalo<sup>55,19</sup>, T. S. Kisner<sup>63</sup>, R. Kneissl<sup>3,5</sup>, L. Knox<sup>22</sup>, H. Kurki-Suonio<sup>19,37</sup>, G. Lagache<sup>81</sup>, J.-M. Lamarre<sup>8</sup>, A. Lasenby<sup>4,57</sup>, R. J. Laureijs<sup>36</sup>, C. R. Lawrence<sup>25</sup>, M. Le Jeune<sup>2</sup>, S. Leach<sup>60</sup>, R. Leonardi<sup>5,36,23</sup>, A. Liddle<sup>18</sup>, M. Linden-Vørnle<sup>3</sup>, M. López-Cañiegos<sup>1</sup>, P. M. Lubin<sup>73</sup>, J. F. Macías-Pérez<sup>1</sup>, B. Ma<sup>56</sup>, D. Maino<sup>27,42</sup>, N. Mandolese<sup>1</sup>, R. Marín<sup>71</sup>, M. Maris<sup>40</sup>, F. Marleau<sup>5</sup>, E. Martínez-González<sup>1</sup>, S. Mas<sup>26</sup>, S. Matarrese<sup>25</sup>, F. Matthäi<sup>64</sup>, P. Mazzotta<sup>20</sup>, A. Melchiorri<sup>26</sup>, J.-B. Melin<sup>12</sup>, L. Mendes<sup>25</sup>, A. Mennella<sup>27,40</sup>, S. Mitra<sup>55</sup>, M.-A. Miville-Deschênes<sup>48,6</sup>, A. Moneti<sup>49</sup>, L. Montier<sup>79,7</sup>, G. Morganté<sup>1</sup>, D. Mortlock<sup>45</sup>, D. Munsh<sup>72,51</sup>, A. Murphy<sup>67</sup>, P. Naselsky<sup>68,31</sup>, P. Natoli<sup>29,2,41</sup>, C. B. Netterfeld<sup>5</sup>, H. U. Nørgaard-Nielsen<sup>1</sup>, F. Noviello<sup>48</sup>, D. Novikov<sup>45</sup>, I. Novikov<sup>68</sup>, S. Osborne<sup>75</sup>, F. Pajot<sup>48</sup>, F. Pasiaff<sup>40</sup>, G. Patanchon<sup>1</sup>, O. Perdereau<sup>62</sup>, L. Perotto<sup>61</sup>, F. Perrotta<sup>20</sup>, F. Piacentini<sup>26</sup>, M. Piat<sup>8</sup>, E. Pierpaoli<sup>7</sup>, R. Piarotti<sup>59,12</sup>, S. Plaszczynski<sup>1</sup>, E. Pointecouteau<sup>1</sup>, G. Polenta<sup>39</sup>, N. Ponthieu<sup>48</sup>, T. Poutanen<sup>37,19,1</sup>, G. W. Pratt<sup>9</sup>, G. Prézeau<sup>65</sup>, S. Prunet<sup>49</sup>, J.-L. Puge<sup>48</sup>, R. Rebolo<sup>3,32</sup>, M. Reinecke<sup>64</sup>, C. Renaud<sup>1</sup>, S. Ricciardi<sup>1</sup>, T. Riller<sup>64</sup>, I. Ristorcelli<sup>79,7</sup>, G. Rocha<sup>58</sup>, C. Rossetti<sup>1</sup>, J. A. Rubiño-Martín<sup>3,32</sup>, B. Rusholme<sup>6</sup>, E. Saar<sup>76</sup>, M. Sandri<sup>1</sup>, D. Santos<sup>49</sup>, B. M. Schaefer<sup>78</sup>, D. Scott<sup>16</sup>, M. D. Seiler<sup>55,8</sup>, G. F. Smoot<sup>21,63,3</sup>, J.-L. Starck<sup>69,12</sup>, F. Stivoli<sup>3</sup>, V. Stolyarov<sup>4</sup>, R. Sunyaev<sup>64,73</sup>, J.-F. Sygnet<sup>1</sup>, J. A. Tauber<sup>1</sup>, L. Terenzi<sup>41</sup>, L. To<sup>61,14</sup>, M. Tomas<sup>27,42</sup>, J.-P. Torre<sup>48</sup>, M. Tristram<sup>62</sup>, J. Tuovine<sup>6</sup>, L. Valenziano<sup>1</sup>, L. Vibert<sup>48</sup>, P. Vielva<sup>54</sup>, F. Villa<sup>41</sup>, N. Vittorio<sup>30</sup>, B. D. Wandelt<sup>49,24</sup>, S. D. M. White<sup>64</sup>, D. Yvon<sup>12</sup>, A. Zacchei<sup>40</sup>, and A. Zonca<sup>23</sup>

(Alliations can be found after the references)

Received 7 January 2011 Accepted 2 July 2011

## ABSTRACT

We present the XMM-Newton follow-up for confirmation of Planck cluster candidates. Twenty-five candidates have been observed to date using snapshot (10 ks) exposures, ten as part of a pilot programme to sample a low range of signal-to-noise ratio (SNR) (4–6), and a further 15 in a programme to observe a sample of SNR > 5 candidates. The sensitivity and spatial resolution of XMM-Newton allows unambiguous discrimination between clusters and false candidates. The 4 false candidates have been identified. A total of 21 candidates are confirmed as extended X-ray sources. Seventeen are single clusters, the majority of which are found to have highly irregular and disturbed morphologies. The remaining four sources are multiple systems, including the unexpected discovery of a supercluster. For 20 sources we are able to derive a redshift estimate from the X-ray Fe K line (albeit of variable quality). The new clusters span the redshift range  $0 < z < 0.54$ , with a median redshift of  $z = 0.37$ . A first determination is made of their X-ray properties including the characteristic size, which is used to improve the estimate of the SZ Compton parameter. The follow-up validation programme has helped to optimise the Planck candidate selection process. It has also provided a preview of the X-ray properties of these newly-discovered clusters, allowing comparison with their SZ properties, and to the X-ray and SZ properties of known clusters observed in the Planck survey. Our results suggest that Planck may have started to reveal a non-negligible population of massive dynamically perturbed objects that is under-represented in X-ray surveys. However, despite their particular properties, the new clusters appear to follow the  $Y_{500}-Y_X$  relation established for X-ray selected objects, where  $Y$  is the product of the gas mass and temperature. Key words. cosmology: observations – galaxies: clusters: general – galaxies: clusters: intracluster medium – cosmic background radiation X-rays: galaxies: clusters

## 1. Introduction

The Planck<sup>1</sup> satellite has been surveying the sky across nine frequencies in the microwave band since August 2009. The resulting data set allows the detection of galaxy clusters through the Sunyaev-Zeldovich (SZ) effect (Sunyaev & Zeldovich 1972). The spectral distortion of the cosmic microwave background (CMB) generated via inverse Compton scattering of CMB photons by the hot electrons in the intra-cluster medium (ICM). The total SZ signal is expected to be closely related to the cluster

Corresponding author: E. Pointecouteau,  
 e-mail: etienne.pointecouteau@irap.omp.eu

<sup>1</sup> Planck (<http://www.esa.int/Planck>) is a project of the European Space Agency (ESA) with instruments provided by two scientific consortia funded by ESA member states (in particular the lead countries: France and Italy) with contributions from NASA (USA), and a scientific consortium led and funded by Denmark.

mass (e.g. da Silva et al. 2004) and its brightness is insensitive to the XMM-LSS survey found 29 systems in 5 days 10 ks redshift dimming. As a result, SZ surveys can potentially provide unbiased cluster samples, covering a wide range of redshifts that are expected to be close to mass-selected. As compared to other SZ instruments, Planck brings a unique nine-band coverage from 30 to 857 GHz and a relatively high, band-dependent spatial resolution of 5–10 arcmin. Most crucially, the Planck SZ survey covers an exceptionally large volume, being the first all-sky survey capable of blindly detecting clusters since the ROSAT All-Sky Survey (RASS) in the X-ray domain. As a consequence, Planck is detecting previously unknown, massive clusters that do not appear in other SZ surveys. Its all-sky coverage allows detection of the rarest clusters, the most massive objects lying in the exponential tail of the mass function. These are the best targets for precision cosmology: their abundance evolution is most sensitive to the cosmological parameters, and their gas mass fractions can be used as distance indicators. In addition, clusters in this high-mass regime are X-ray bright, making their observation easier, and their ICM is expected to be the least affected by non-gravitational processes. These newly-discovered Planck clusters will thus also be ideal targets for studying the physics of the gravitational collapse that drives all cluster formation.

The Planck survey is providing a sample of cluster candidates. Any such survey sample is expected to include a fraction of false detections, due for example to fluctuations in the complex microwave astrophysical sky. In addition, as a result of Planck's moderate spatial resolution at SZ frequencies with respect to typical cluster sizes, Planck cluster candidate measurement essentially provides only coordinates and total flux estimates; these estimates are further hampered by the size degeneracy discussed extensively in the literature. A vigorous follow-up programme is therefore required to scientifically exploit Planck cluster candidate data. Such a programme includes candidate confirmation, which is a non-trivial part of the catalogue validation, in addition to redshift measurement, estimation of relevant physical parameters (including cluster size, allowing precise SZ flux estimates), and investigation of scaling properties. In particular, measurement of the function and for related cosmological applications.

The all-sky nature of the Planck survey means that confirmation and redshift measurement of cluster candidates is not a trivial task. In the optical domain, the only publicly available large survey is the Sloan Digital Sky Survey (SDSS), although cross-correlation with this survey can be used to confirm redshifts up to  $z \approx 0.6$ , it covers only part of the northern sky. Furthermore, optical confirmation is hampered by the relatively large Planck source position uncertainty, which can be up to 5 arcmin. To discriminate between a true redshifted cluster and a chance association with low-mass systems, spectroscopic redshift or photometric redshift estimates with a wide-field, multi-band, instrument are required.

In contrast, confirmation in X-rays offers definite advantages. Above the Galactic Plane, the detection of extended X-ray emission is an unambiguous signature of a cluster, and the density-squared dependence of the X-ray emission reduces projection effects nearly to zero. Furthermore, the low space density of groups and clusters in a typical X-ray exposure makes spurious association with Planck candidate unlikely. For instance,  $R_{500}$

<sup>2</sup> <http://www.sdss.org/>

## 2. The XMM-Newton validation follow-up of Planck cluster candidates

### 2.1. The Planck survey

Planck (Tauber et al. 2010; Planck Collaboration 2011) is the third generation space mission to measure the anisotropy of the CMB. It observes the sky in nine frequency bands covering 30–857 GHz with high sensitivity and angular resolution from 31' to 5'. The Low Frequency Instrument (LFI; Mandolesi et al. 2010; Bersanelli et al. 2010; Mennella et al. 2011) covers the 30, 44, and 70 GHz bands with amplifiers cooled to 20 K. The High Frequency Instrument (HFI; Lamarre et al. 2010; Planck HFI Core Team 2011) covers the 100, 143, 217, 353, 545, and 857 GHz bands with bolometers cooled to 0.1 K. Polarisation is measured in all but the highest two bands (Usahy et al. 2010; Rosset et al. 2010). A combination of radiative cooling and three mechanical coolers produces the temperatures needed for the detectors and optics (Planck Collaboration 2011). Two data processing centres (DPCs) check and calibrate the data and make maps of the sky (Planck HFI Core Team 2011; Zacchei et al. 2011). Planck's sensitivity, angular resolution, and frequency coverage make it a powerful instrument for Galactic and extragalactic astrophysics as well as cosmology. Early astrophysics results are given in Planck Collaboration (2011h–z).

### 2.2. Blind detection of SZ clusters in Planck

The blind search for clusters in Planck data relies on a multi-matched filter (MMF) approach (Melin et al. 2006)<sup>3</sup>. This detection algorithm operates on all-sky maps divided into a set of overlapping square patches, using simultaneously the 6 frequency maps of the HFI instrument (Planck Collaboration 2011d). Within the algorithm, the SZ spectral signature and the universal pressure profile derived by Arnaud et al. (2010) are used as spectral and spatial templates, respectively. In such a blind search, the position, the characteristic scale of the profile ( $R_{500}$ ) and the amplitude ( $Y_{500}$ ) are left free, being optimised by the MMF algorithm. In practice the algorithm is run in an iterative way: after a first detection run to locate candidates, consecutive runs on sky patches centred on the candidate positions refine the estimated signal-to-noise ratio ( $S/N$ ) and other properties.

Cluster candidates then undergo a validation process, extensively described in Planck Collaboration (2011d). This process includes internal quality checks (e.g., map artefacts, cross-comparison between detection algorithms, SZ spectral signature, astrophysical contamination by Galactic dust, point sources or structures in the CMB) and cross-correlation with ancillary data and catalogues allowing known clusters to be identified. This process produces a list of new Planck SZ cluster candidates above a given  $S/N$  threshold ( $S/N = 4$  in this work).

### 2.3. XMM-Newton target selection

From the list of new potential clusters detected as SZ sources in the Planck survey, we selected 25 targets in a two step process:

1. Pilot programme: 10 targets were selected on the basis of the Planck survey as it stood at the end of October 2009, i.e. 62% sky coverage. These targets were explicitly chosen to

sample the lower range of signal-to-noise ( $S/N < 6$ ) in order to better characterise the nature and quality of the SZ signal.

2. High  $S/N$  programme: a further 15 targets were chosen in the spring of 2010 when the first full-sky coverage was close to completion (95% sky coverage). In contrast to the pilot programme, here we focused on high-significance SZ sources ( $S/N > 5$ ) and selected candidates starting from the highest  $S/N$ .

In both cases the selection process was intimately linked to the Planck HFI data time ordered information processing status, calibration, attitude and map versions (as of Dec. 7, 2009 and April 19, 2010 for the two programmes, respectively). The choice of targets was also constrained by the XMM-Newton visibility in a period of 2–3 months following their submission to the science operations centre. For both programmes, maps and spectra of each potential target were visually inspected, including re-processing with aperture photometry methods. Cross-correlation with the RASS Bright Source Catalogue (RASS-BS; Ogles et al. 1999) and Faint Source Catalogue (RASS-FS; Ogles et al. 2000) was undertaken. For the two targets of the pilot programme falling in the SDSS area, we ran a dedicated algorithm to search for galaxy overdensities (Fromenteau et al., in prep.), allowing us to track significant concentrations of matter down to  $z \approx 0.6$ . These two targets were chosen to test the SDSS based confirmation at high  $z$ . The first candidate, PLCK G070.8–21.5, was not confirmed (see Fromenteau et al., in prep., for discussion); the other candidate, PLCK G214.37–0.0, is discussed in Sect. 7.2.1. Detailed searches in XMM-Newton, Chandra and Suzaku observatory logs were also undertaken in order to avoid duplication of performed or accepted observations with similar facilities.

Six of the ten pilot programme targets were confirmed (see Table 1); two of these are multiple systems. Taking into account the result of the pilot project, for the second programme we set a lower  $S/N$  threshold of  $S/N = 5$  and refined and strengthened the selection criteria. In particular, we required that the source be independently detected by at least two of the three blind detection methods, and more quality flags were considered. The internal checks were very similar to those defined for constructing the early SZ (ESZ) sample (Planck Collaboration 2011d) which benefit from the result of the XMM-Newton Pilot programme. We also performed a search for emission in the RASS hard band images, looking for X-ray signatures beyond those recorded in the RASS source catalogues. However, RASS information never took precedence over the internal Planck quality flags. Note that two of the false candidates of the Pilot programme (PLCK G343.4–43.4 and PLCK G226.1–16.9) were associated with a RASS-FSC source in XMM-Newton subsequently revealed to be several point sources (see Sect. 3.2). Thus association with an RASS source alone is not sufficient for cluster candidate confirmation.

The ESZ sample (Planck Collaboration 2011c) consists of a high signal-to-noise, i.e. primarily  $S/N \geq 6$ , list of 189 clusters and cluster candidates based on data from the first 10 months of the Planck survey. Ten of the 21 objects presented in the present paper passed the ESZ selection criteria and are thus part of the ESZ sample released to the community in January 2011. The original  $S/N$  of their detection in the Planck maps is given in Table 1, whereas the  $S/N$  values provided in Table 2 are derived from the 10 month Planck maps on the basis of which the ESZ sample was constructed.

<sup>3</sup> Results from other methods have been cross-compared to those from the MMF search, including from the PowellSnakes-based algorithm (Carvalho et al. 2009).

Table 1. Observation log of the XMM-Newton validation follow-up.

Name	SN	RA <sub>SZ</sub> (deg)	Dec <sub>SZ</sub> (deg)	OBSID	Filter	t <sub>exp</sub> (ks EPN)	Clean fraction (MOS/EPN)	Con rmed
PLCK G277.5-51.7	6.1	43.596	-58.964	0656200301	THIN	16.5	/0.25	Y ESZ
PLCK G334.5-38.0*	4.9	313.177	Š61.202	0656200701	THIN	21.2	/0.85	Y
PLCK G250.0-24.1	4.9	143.042	Š17.647	0656200401	THIN	10.4	/0.0	Y
PLCK G286.5-38.4	4.7	59.800	Š72.067	0656200501	THIN	13.6	/0.07	Y
PLCK G004.5-19.5	4.6	289.226	Š33.509	0656201001	MED	10.0	/0.16	Y
PLCK G214.0-36.9*	4.2	137.206	14.642	0656200101	THIN	17.6	/0.7	Y
PLCK G070.5-21.5	4.1	321.410	19.941	0656200201	MED	25.4	/0.14	...
PLCK G317.5-54.1	4.1	355.247	Š61.038	0656200801	THIN	12.0	/0.97	...
PLCK G226.5-16.9	4.0	93.139	Š19.040	0656200601	THIN	10.0	/0.74	...
PLCK G343.5-43.4	3.9	320.145	Š53.631	0656200901	MED	10.0	/0.99	...
PLCK G287.0-32.9	10.2	177.714	Š28.074	0656201201	THIN	10.0	/0.74	Y ESZ
PLCK G171.5-40.7	10.7	48.231	8.380	0656201101	THIN	10.0	/0.8	Y ESZ
PLCK G285.5-23.7	8.3	110.805	Š73.457	0656201401	THIN	10.0	/0.96	Y ESZ
PLCK G271.5-31.0	8.3	87.315	Š62.087	0656201301	THIN	10.0	/1	Y ESZ
PLCK G262.5-40.9	7.4	69.624	Š54.309	0656201601	THIN	14.7	/0.19	Y ESZ
PLCK G308.5-20.2*	7.4	229.588	Š81.523	0656201501	THIN	10.0	/1	Y ESZ
PLCK G337.5-26.0*	6.4	288.583	Š59.513	0656201701	THIN	13.7	/1	Y ESZ
PLCK G292.5-22.0	6.2	180.241	Š39.889	0656201801	MED	13.2	/0.65	Y ESZ
PLCK G205.5-63.0	6.1	41.593	Š20.527	0656201901	THIN	11.7	/1	Y
PLCK G241.5-28.7	5.9	85.768	Š36.022	0656202001	THIN	10.0	/1	Y
PLCK G286.5-31.3	5.9	82.8430	Š75.164	0656202101	THIN	10.0	/0.73	Y ESZ
PLCK G018.7-23.6	5.6	255.553	Š1.004	0656202201	THIN	7.2	/1	Y
PLCK G100.5-30.4	5.5	350.589	28.563	0656202301	THIN	10.0	/0.79	Y
PLCK G272.9-48.8	5.1	173.310	Š9.479	0656202601	THIN	11.7	/0	Y
PLCK G285.5-17.2	5.2	130.956	Š71.190	0656202501	THIN	10.0	/1	Y ESZ

Notes. The 10 targets of the pilot programme are listed first. Column (1): Planck source name. Asterisked objects denote sources that were found to be multiple systems in X-rays. Column (2): signal-to-noise ratio of the detection of a Planck cluster candidate in the version of the Planck-HFI maps available for each programme. Columns (3) and (4): right ascension and declination of the source (J2000). Columns (5)–(8): XMM-Newton observation identification number, filter used, on-source exposure time with the camera and fraction of useful time after cleaning for periods of high background due to soft protonares (and camera, see also Serfaty et al. 2015). Column (9): confirmed clusters are flagged. Those included in the ESZ sample (Planck Collaboration 2011a) are also identified.

#### 2.4. Observation setup

As discussed by Scharf (2002), the optimum energy band for XMM-Newton cluster detection is the soft energy band (energy below 2 keV), for which the signal-to-noise ratio reaches a maximum. We calculated expectations for XMM-Newton sensitivity in that band for two representative values of the SZ flux from within  $R_{500}$ :  $Y_{500} = 5 \times 10^{-4} \text{ arcmin}^{-2}$  and  $Y_{500} = 2 \times 10^{-3} \text{ arcmin}^{-2}$ . In each case, the expected cluster luminosity  $L_{500}$  for various redshifts was estimated using the  $L_{500}-D_A Y_{500}$  relation of Arnaud et al. (2010), assuming self-similar evolution. We then derived the corresponding XMM-Newton count rates,  $R$ , in the [0.3–2] keV band for the MOS-CCD (hereafter MOS) and pn-CCD (hereafter pn) camera (Turner et al. 2001; Strüder et al. 2001). We used the xspec software (Arnaud 1996) to simulate an absorbed thermal model (assuming  $kT = 7 \text{ keV}$ ,  $N_H = 2 \times 10^{20} \text{ cm}^{-2}$ ), convolved with the instrument response. The corresponding angular extent  $\theta_{500}$  was estimated from the  $L_{500}-M_{500}$  relation of Pratt et al. (2009). The signal-to-noise ratio of the detection is then given by  $SN = (R \cdot t_{\text{exp}}) / (R + (2R_{\text{bkg}} A))$ , where  $t_{\text{exp}}$  is the exposure time,  $R_{\text{bkg}}$  is the background count rate, and  $A = 4 \pi \theta_{500}^2$  is the integration area in square arc minutes. We assumed a [0.3–2] keV band background count rate  $R_{\text{bkg}} = 4.5 \times 10^{-3} \text{ counts s}^{-1} \text{ arcmin}^{-2}$ , as estimated from the blank sky backgrounds of Read & Ponman (2003). Figure 1 shows the

resulting SN of an XMM-Newton detection as a function of redshift.

Since the goal of the XMM-Newton observations is confirmation of new Planck SZ cluster candidates, the nominal observing time was set to 10 ks (net camera time) per target. Such a snapshot observation is sufficient to detect the cluster – if real – at better than 10 up to  $z = 1.5$  (Fig. 1). The nominal setup used the THIN filters (unless optical loading had to be avoided) and EFF mode for the camera. The boresight was optimised to avoid camera gaps.

#### 2.5. XMM-Newton data reduction

We produced calibrated event lists using v10.0 of the XMM-Newton science analysis system (SAS). Observations were cleaned for periods of high background due to soft protonares, -selected and corrected for vignetting as described in Pratt et al. (2007). Point sources were identified from the small scales of wavelet-decomposed images in the [0.2] and [2.5] keV bands. These sources were excluded in the analysis of confirmed clusters, with the exclusion radius matched to the point spread function (PSF) size (which varies across the detector).

Above 2 keV the XMM-Newton background is dominated by particle events. We subtracted this background using a

stacked event list built from observations obtained with the Iter wheel in the position, recast to the pointing position and renormalised using the count rate in the high energy band free of cluster emission. The remaining background (due to the cosmic X-ray background of unresolved AGN and Galactic emission) was estimated from the particle-background subtracted emission from an annulus beyond the cluster emission. For the spectral analysis, we modeled this background emission as arising from two thermal sources and a power-law source with index 1.4, taking into account the absorbing Galactic column density in the direction of the object (see, e.g. De Luca & Molendi 2004).

As Table 1 shows, the observations are of variable quality. In three cases the data were completely contaminated by soft proton flares and formally had no useful observing time. For two of these observations, the data were completely contaminated too. In these instances, we used data only (uncleaned in the last two cases). The power-law index in the background model was left free, which empirically produces a relatively good fit to the background spectrum. The spectroscopic results for these objects should be treated with caution.

Spectral fits were undertaken in the [0–10] keV energy range, after binning the spectra to a minimum of 25 counts per bin and excluding background fluorescence line regions. The cluster component was modelled with an absorbed model with the reference solar abundances from the data of Anders & Grevesse (1989). The hydrogen column density,  $N_H$ , was fixed at the 21 cm value from Dickey & Lockman (1990), except for PLCK G286.338.4, PLCK G308.320.2 and PLCK G018.723.6. Their best fit  $N_H$  values were found to be significantly higher by a factor 1.8, 1.8 and 2.4, respectively. These clusters are located at low latitude, in regions of high IR dust emission (Snowden et al. 1997 Fig. 11). The 21 cm value may underestimate the total  $N_H$ , measured from X-ray data, due to a non-negligible  $H_2$  contribution. To check this hypothesis, we used the IRIS maps (Viville-Deschênes & Lagache 2005) as tracers of the dust emission and the correlation between the Galactic dust emission and the total hydrogen column density (Boulanger et al. 1996) to estimate the  $N_H$  values at the cluster locations (see Pointecouteau et al. 2004). A better agreement was found with X-ray values, with ratios of 1.30, 1.06 and 1.48. It must also be noted that the PLCK G286.338.4 observation is highly contaminated by solar flares and only data are used. Some residual background may also affect the low energy part of the spectrum and thus the  $N_H$  estimate.

### 3. XMM-Newton validation: methods and outcome

The observations were completed by the end of October 2010. The median clean observation time is 7 ks (Table 1). Of 25 targets, 21 are confirmed as X-ray extended sources. Only four targets with  $SN < 4.1$  were not confirmed. The confirmation status of each XMM-Newton observation is given in Table 1.

#### 3.1. Confirmed cluster candidates

Our procedure for candidate cluster confirmation consists of identifying an extended X-ray source coincident with a Planck SZ source and checking that the SZ and X-ray properties are consistent. Generally, a candidate cluster (or supercluster) is clearly visible within 5' of the Planck candidate position, in 17 systems show extended emission from a single source and are confirmed as new clusters of galaxies. Using the Fe K line in the X-ray spectrum we have estimated a redshift for all these objects, albeit with large uncertainties in some cases (see Sect. 4.1). We have also calculated the  $Y_{500}$  parameter (Sect. 5.1). A final check of the candidate confirmation is the good agree-

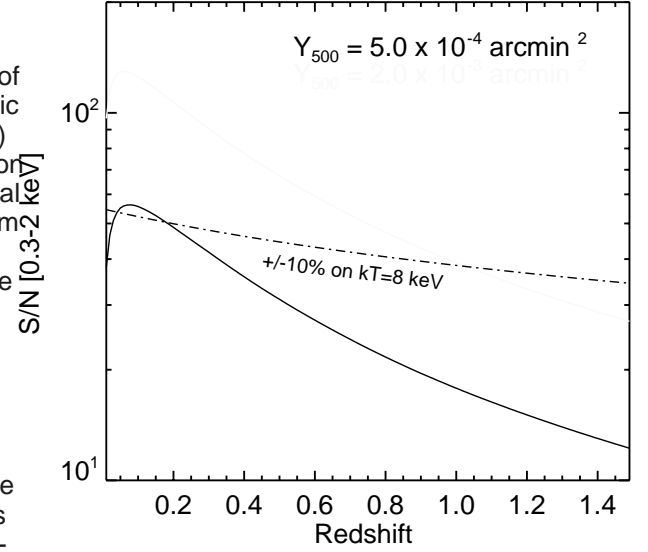


Fig. 1. Sensitivity of XMM-Newton observations to typical Planck SZ sources. The expected signal-to-noise ratio (SN) of the cluster detection in the [0.3–2] keV energy band with the camera is plotted as a function of redshift for an exposure time of 10 ks assuming two typical SZ fluxes. See text for details of the model assumed to convert SZ to X-ray flux and count rate. The dash-dotted line indicates the SN required for 10% uncertainty on the temperature measurement of an 8 keV cluster.

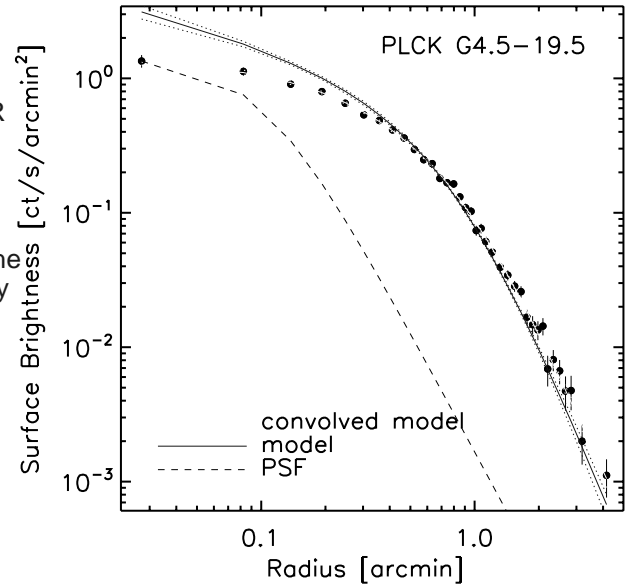


Fig. 2. Surface brightness profile of PLCK G4.5–19.5 at  $z = 0.54$ , the highest  $z$  cluster of the sample, as measured with XMM-Newton. The data of the 1/2 and camera in the [0.3–2] keV energy band are combined. The green line indicates the best fitting model (see text); the red line is the best fitting model convolved with the point spread function (PSF) of XMM-Newton and the dashed line is the on axis XMM/PSF, normalised to the central intensity. The source is clearly extended.

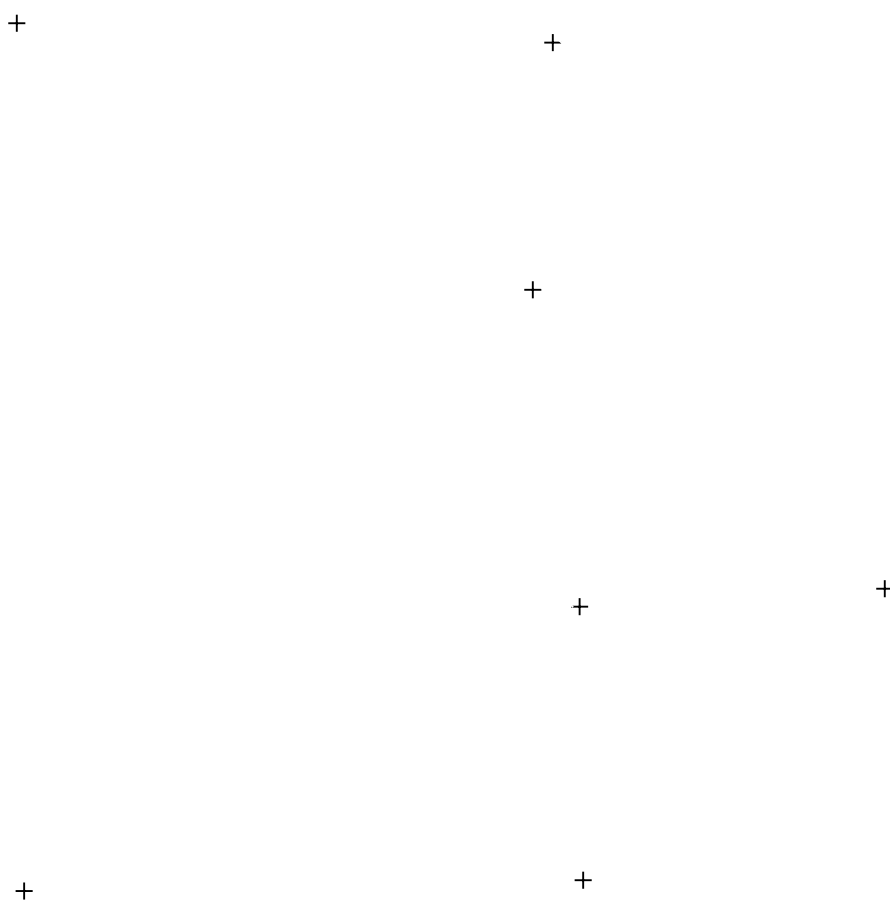


Fig. 3. XMM-Newton images of all confirmed cluster candidates, except for the two triple systems which are shown in Fig. 12 and discussed in Sect. 7, in the [0.3–2] keV energy band. The observations of PLCK G272.88 and PLCK G250.024.1 suffer from high background that has only been crudely subtracted. Image sizes are 30" on a side, where  $\theta_{500}$  is estimated from the  $M_{500}-Y_X$  relation (see Sect. 5.1). Images are corrected for surface brightness dimming with divided by the emissivity in the energy band, taking into account galactic absorption and instrument response, and scaled according to the self-similar model. The colour table is the same for all clusters, so that the images would be identical if clusters obeyed strict self-similarity. The majority of the objects show evidence for significant morphological disturbance. A yellow cross indicates the Planck position and a red green plus sign the position of a RASS-BSC source.

ment found between the measured SZ signal and that expected from the  $Y_X$  value (Sect. 5.1). A further two confirmed candidates were revealed to be double systems, one of which is a projection of two independent clusters at different redshifts. More unexpected are two additional newly-discovered triple systems. The XMM-Newton images of confirmed single and double multiple clusters are discussed in more detail in Sect. 7. In each panel, the Planck source centre position is marked with a cross; in addition, when rele-

vant a red green plus sign shows the associated RASS/BSC source.

### 3.2. False cluster candidates

In some cases a source is not clearly visible in the image and then the relatively large FWHMs of the HFI beams (55.9; Planck HFI Core Team 2011) complicate source search and confirmation. For these observations we employ the approach described in Suhada et al. (2010), applying the XMM-Newton SAS source detection algorithm `sboxdetect` and `emldetect` to the images to determine whether an extended source lies within the Planck beam. In brief, images are produced in the [0.35–24] keV band and `sboxdetect` is first run in local mode, where the background is estimated locally for each source. Sources found in this first step are then excised, leaving an image suitable for background estimation. The background image is modeled with two components, a vignettted component to represent the X-ray background, and a non-vignettted component to represent the particle and instrumental background. The model is based on a linear combination of two templates based on vignettted and non-vignettted exposure maps, and is fit to the source-subtracted image. We then re-`sboxdetect` with this model background. All sources found in this step are then analysed with the maximum likelihood (ML) task `emldetect`, that analyses each source by fitting with a 2D King function convolved with the PSF. The log of the detection likelihood of each source as defined in the code  $\log_{10} \text{det\_ml} = \ln P_{\text{rand}}$ , where the latter is the probability of the observed counts arising from Poisson fluctuations. We set the minimum  $\log_{10} \text{det\_ml} = 6$ , corresponding to a 3 detection. In addition to the above, we also searched for possible extended sources using visual inspection of a wavelet-smoothed image.

Figure 4 illustrates application of the method for the false source PLCK G226.1-16.9. This candidate was the lowest SNR candidate of the Pilot sample ( $S = 4.0$ ) and located close to a RASS-FSC source, which may have been the cluster counterpart. The top panel shows the raw XMM-Newton image and the reconstructed ML source image. The RASS-FSC source located at 0.8 from the Planck source is clearly detected with XMM-Newton (red plus sign in the top panels). The surface brightness profile is well fitted by a point source convolved with the XMM-Newton PSF (bottom left panel). The source spectrum is clearly a power law, and thermal emission from a 0.3 solar abundance ICM is rejected at high confidence at all redshifts and temperatures. This source is most likely an AGN and is definitively not the Planck counterpart.

The source list produced by the ML method includes two potentially extended sources, only one of which is within 5 of the Planck source position (source labelled A in the figure). It is located 0.8 from the RASS-FSC source position and is much fainter, showing the capability of XMM-Newton to separate sources. The source has an estimated [0.35–24] keV flux of  $2 \times 10^{-14} \text{ erg cm}^{-2} \text{ s}^{-1}$ , which is more than 5 times lower than that expected from the SZ source even if located at  $z = 1.5$ . Furthermore its extent (although not well constrained) is small and it is perfectly coincident with a 2MASS galaxy. This source again could not be the Planck counterpart. Finally, from a wavelet-smoothed image, there was a hint that another source, located 0.5 away from the Planck candidate position,

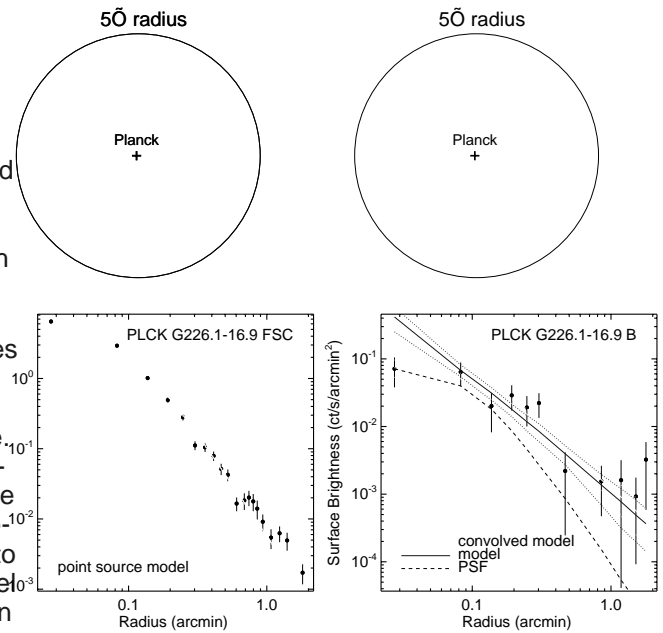


Fig. 4. Illustration of the XMM-Newton validation procedure results for a false candidate, PLCK G226.1-16.9. Top panels: sum of the raw image (left) and reconstructed image (right) in the soft band. The circle of 5 radius centred on the Planck position (green cross) corresponds to the conservative position error box. The RASS-FSC source is clearly detected (red cross) as a point source: its surface brightness profile (black points in left bottom panel) is well fitted by the XMM-Newton PSF (red line). Two extended sources labelled A and B are also detected. Bottom right panels same as Fig. 2 for source B.

was extended, although it was not classified as such with the ML method (source labelled B). We extracted its profile and confirmed it as extended, although the extent was not very significant (bottom right panel of Fig. 4). However, its flux was half that expected from the observation. But Planck flux, even for a cluster at  $z = 1.5$ . Nevertheless, in view of possible errors in Planck position, we re-analysed the Planck data by re-extracting the signal exactly at the position of the source. The SZ detection was no longer significant, leading us to conclude that source B was definitively not the counterpart to the Planck candidate. From the XMM-Newton observation we thus concluded that the Planck candidate was a false detection.

## 4. Redshift estimate

### 4.1. XMM-Newton estimates

The ICM has a typical abundance  $\sim 30$  times solar, implying that metals are present in large amounts (Salestra et al. 2007; Leccardi & Molendi 2008; Maughan et al. 2008; or recent work on metals in the cluster context). The spectroscopic sensitivity of XMM-Newton allows the measurement of the intensity and centroid energy of the strongest line emission, namely the Fe K and Fe L line complexes (respectively found at 6.4 and 1 keV at  $z = 0$ ). As a consequence the Fe line emission can be used to constrain the cluster redshift. We have thus searched for their signature in the XMM-Newton observations, focusing mainly on the Fe K complex, which is about 10 times as strong as any other line emission in the ICM. A clear detection then provides an estimate of the X-ray redshift.

The intrinsic spectral resolution of XMM-Newton is  $E = 150 \text{ eV}$  at 64 keV and  $E = 100 \text{ eV}$  at 32 keV; the ener-

<sup>4</sup> See

<http://xmm.esac.esa.int/sas/current/doc/emldetect/node3.html> for more details



gies here correspond to the Fe K complex centroid energy. Finally, the source PLCK G262540.9 appeared to be one of the a cluster at a redshift of  $z = 0$  and  $z = 1$ , respectively. Such res-ACT SZ optically-confirmed clusters (Menanteau et al. 2010) olution allows centroid determination to typically 10–15 eV for accepted for observation by Chandra after it was scheduled for high quality spectra, of the same magnitude as the systematic observation with XMM-Newton. The reported photometric red-certainty of the calibration of the energy reconstruction (about  $z_{\text{phot}} = 0.54 \pm 0.05$ , in disagreement with our X-ray-5 eV and 10 eV in the central CCD of the and cam-derived value of  $z_{\text{Fe}} = 0.38$  at the 3 level. Although slightly era, respectively). The overall energy uncertainty would yield weak, the Fe K line is clearly seen in the X-ray spectrum (see a typical corresponding redshift uncertainty of 0.002. In Fig. 5 right panels). We thus adopt the X-ray estimate. However, practice, the limiting factor affecting the accuracy of the red-optical spectroscopic observations are clearly needed to confirm shift determination is the statistical uncertainty in the spectrum of the cluster redshift. All compiled and derived optical redshifts which is linked to the observation duration and overall quality are reported in Col. 6<sub>(opt)</sub> in Table 2. (background conditions). Furthermore, Planck detected clusters are mostly massive, hot objects with low Fe K line equivalent widths (Rothenflug & Arnaud 1985). This makes  $z_{\text{Fe}}$  determination more difficult than for cooler objects.

To estimate  $z_{\text{Fe}}$  using xspec we first performed a spectral fit of the region corresponding to the maximum significance of the detection (defined from the surface brightness profile in the soft band), with the redshift as one of the free parameters. The abundance was left free to fit within a typical cluster range (0.2–0.6 times solar). From this starting point we investigated the  $\chi^2$  in the  $kT$ – $z_{\text{Fe}}$  plane using a regular grid. The best fitting  $kT$  and  $z_{\text{Fe}}$  values were recovered from a simple maximum likelihood analysis, whereupon these best fitting values were used as input for a final spectral fit. When a two- or three-peak degeneracy appeared in the  $kT$ – $z_{\text{Fe}}$  plane, we checked the various potential  $z_{\text{Fe}}$  values and chose the redshift giving the best spectral fit as defined by the  $\chi^2$  and the null probability hypothesis.

This redshift estimation process is illustrated by three cases in Fig. 5 with the left panel showing a fully degenerate case, the middle panel a double-peaked case and the right panel a well constrained case. These redshifts are tagged with quality values  $Q_z = 0, 1, 2$ , respectively, in Table 2. The few cases where no redshift estimate was possible are tagged with  $Q_z = -1$ .

#### 4.2. Optical estimates

For three clusters, we have estimated the redshift either from existing optical archive observations or dedicated follow-up observations as part of the overall Planck cluster candidate validation programme. The most recent corresponds to telescope time acquired by the Planck consortium at the ENO telescopes, Observatorio del Teide (Tenerife, Spain – AO 2010A and 2010B). The details of the observation setup and data processing can be found in Appendix A.1.

- PLCK G100.530.4. The source was observed in 4 bands (griz) with the CAMELOT camera at the 0.82-m IAC80 telescope. After data reduction, we derived a photometric redshift of  $z_{\text{phot}} = 0.38 \pm 0.04$ , using the code Benítez 2000. This estimate is compatible within 3 $\sigma$  with the  $z_{\text{Fe}} = 0.31$  derived from the X-ray spectroscopy.
- PLCK G285.623.7. We reduced the ESO NTT/SUSI2 archive images for this object, deriving a red-sequential redshift of  $z_{\text{phot}} = 0.37$ . This estimate is in good agreement with the X-ray spectroscopic redshift  $z_{\text{Fe}} = 0.39$ .
- PLCK 286.538.4. ESO NTT/SUSI2 images and NTT/EMMI spectroscopic archive data targetting the X-ray source RX J0359.67205 were available. From a poor quality NTT/EMMI spectrum, we extracted a redshift of  $z_{\text{dec}} = 0.307 \pm 0.003$ , backed-up by the presence of two absorption line features (H and Mg). Again this value agrees well with highly disturbed object at  $z = 0.09$ , the lowest of the sample, the X-ray spectroscopic redshift  $z_{\text{Fe}} = 0.31$ .

#### 5. Physical parameter estimates of confirmed clusters

##### 5.1. XMM-Newton data

For all single clusters (17 systems) or obvious sub-components in double and triple systems (4 objects), the X-ray peak position was taken to be the (sub-)cluster centre. For these systems we undertook a more in-depth analysis assuming that a spherically symmetric approximation is appropriate.

Surface brightness profiles, centred on the X-ray peak, were extracted in the [0.3–2] keV band in 33 bins. Deprojected, PSF-corrected gas density profiles were then calculated using the method described in Croston et al. (2008). Global cluster parameters were then estimated self-consistently with  $R_{500}$  via iteration about the  $M_{500}$ – $Y_X$  relation of Arnaud et al. (2010, see also Pratt et al. 2010) viz.,

$$E(z)^{2/5} M_{500} = 10^{14.567 \pm 0.010} \frac{Y_X}{2 \times 10^{14} \text{ M keV}}^{0.561 \pm 0.018} h_{70}^{51} M, \quad (1)$$

assuming the standard evolution predicted by the self-similar model purely based on gravitation. In addition, the X-ray luminosity in the [0.15–2.4] keV band interior to  $R_{500}$ ,  $L_{500}$  was calculated as described in Pratt et al. (2009). All resulting X-ray properties are summarized in Table 2. Errors include only statistical uncertainties. We did not attempt to include systematic errors due to redshift uncertainty or high background level; such estimates are beyond the scope of the paper. The results for this sample are not used for quantitative statistical study (e.g. derivation of scaling laws), which would require redshift confirmation (sources with  $Q_z < 2$ ) and deeper XMM-Newton observations.

The X-ray position for single systems is compared to the Planck position in Fig. 6. The offset behaviour is similar to that observed for known clusters in the ESZ sample (Planck Collaboration 2011, for discussion). Except for the outlier PLCK G18.723.6, the positional offset is less than 2 arcmin and is clearly dominated by the Planck reconstruction error which peaks at that value. A physical offset is also expected, especially for merging clusters. Such an offset would contribute less with increasing  $z$  as it would be more and more poorly resolved. The small residual systematic variation of the offset with  $z$ , for  $z > 0.2$ , suggests that physical offsets may indeed slightly contribute. This is likely to be the case for PLCK G18.723.6, a highly disturbed object at  $z = 0.09$ , the lowest of the sample, and which has an offset of 3 corresponding to  $0.3 R_{500}$ . In all

Table 2. X-ray and SZ properties of the confirmed Planck sources.

Name	SN	RA <sub>X</sub>	Dec <sub>X</sub>	z <sub>Fe</sub>	z <sub>opt</sub>	Q <sub>X</sub>	R	det	R <sub>500</sub>	T <sub>X</sub>	M <sub>gas500</sub>	Y <sub>X</sub>	Y <sub>500</sub>	M <sub>500</sub>	L <sub>500</sub>
		[h:m:s]	[d:m:s]				[cts s <sup>-1</sup> ]	[ ]	[kpc]	[keV]	[10 <sup>14</sup> M <sub>⊙</sub> ]	[10 <sup>14</sup> M <sub>⊙</sub> keV]	[10 <sup>54</sup> Mpc <sup>2</sup> ]	[10 <sup>14</sup> M <sub>⊙</sub> ]	[10 <sup>44</sup> erg s <sup>-1</sup> ]
PLCK G285.5-23.7	11.5	07:23:18.4	Ŝ3:27:20.6	0.39	0.37	2	1.85±0.02	4.1	1216	6.9±0.74	1.23±0.04	8.62±1.28	1.27±0.35	7.71±0.50	16.91±0.27
PLCK G287.9-32.9	10.6	11:50:49.2	Ŝ28:04:36.5	0.39	...	1	2.6±0.01	6.8	1541	12.8±0.42	2.39±0.03	30.6±0.36	3.30±0.16	15.72±0.27	17.20±0.11
PLCK G171.5-40.7	10.6	03:12:57.4	08:22:10.3	0.27	...	2	2.4±0.03	5.3	1428	10.6±0.42	1.43±0.04	15.2±0.72	2.05±0.21	10.92±0.37	11.28±0.19
PLCK G271.5-31.0	8.5	05:49:19.5	Ŝ62:05:16.0	0.37	...	2	3.3±0.01	5.2	1212	7.9±1.23	1.02±0.04	8.0±1.03	1.02±0.17	7.47±0.70	18.95±0.16
PLCK G262.5-40.9	8.3	04:38:17.2	Ŝ54:19:25.1	0.39	0.54	2	1.72±0.02	5.6	1169	7.7±0.87	0.90±0.06	7.01±0.98	1.14±0.22	6.87±0.68	9.94±0.47
PLCK G277.5-51.7	7.4	02:54:16.7	Ŝ58:56:44.0	0.44	...	1	1.3±0.02	5.8	1172	6.3±0.84	1.26±0.02	8.01±0.57	1.70±0.20	7.32±0.38	9.46±0.07
PLCK G286.5-31.3	6.9	05:31:27.5	Ŝ75:10:41.2	0.21	...	2	1.8±0.04	4.6	1149	6.8±0.94	0.60±0.07	4.14±3.01	0.61±0.32	5.32±0.86	3.72±0.23
PLCK G292.5-22.0	6.9	12:01:05.3	Ŝ39:52:26.2	0.30	...	2	1.4±0.03	6.8	1336	9.8±0.84	1.17±0.04	11.4±1.33	1.45±0.24	9.25±0.60	5.46±0.09
PLCK G285.5-17.2	6.3	08:43:44.4	Ŝ71:13:13.7	0.35	...	1	0.6±0.02	4.4	1044	4.8±0.35	0.71±0.01	3.4±0.40	0.79±0.13	4.67±0.22	4.45±0.08
PLCK G18.7-23.6	6.6	17:02:21.3	Ŝ00:59:58.9	0.09	...	2	3.9±0.01	10.5	1034	4.6±0.32	0.39±0.02	1.8±0.32	0.32±0.17	3.42±0.22	1.21±0.05
PLCK G4.5-19.5	5.9	19:17:04.6	Ŝ33:31:21.9	0.54	...	2	1.2±0.02	4.8	1245	10.3±0.52	1.37±0.03	14.27±0.87	1.99±0.20	9.88±0.35	17.78±0.11
PLCK G241.5-28.7	5.7	05:42:56.8	Ŝ35:59:54.8	0.42	...	2	0.9±0.02	3.6	1065	6.0±0.32	0.75±0.02	4.5±0.39	0.79±0.11	5.37±0.20	6.72±0.12
PLCK G272.9-48.8	5.4	11:33:10.5	Ŝ09:28:52.2	0.40	...	2	0.6±0.01	3.7	1053	4.6±0.32	0.88±0.02	4.0±0.32	0.87±0.18	5.07±0.21	12.36±0.09
PLCK G205.5-63.0	5.3	02:46:25.8	Ŝ20:33:16.9	0.31	...	2	1.1±0.03	5.5	1111	6.0±0.39	0.72±0.02	4.38±0.30	0.83±0.09	5.37±0.21	3.89±0.08
PLCK G250.0-24.1	5.2	09:32:13.8	Ŝ17:38:06.7	0.40	...	0	0.1±0.02	3.8	1061	6.7±0.28	0.63±0.03	4.27±0.42	0.72±0.12	5.19±0.21	3.37±0.19
PLCK G286.5-38.4	5.1	03:59:10.2	Ŝ72:04:46.1	0.31	0.30 <sup>(a)</sup>	2	0.32±0.05	4.5	1064	5.6±0.14	0.62±0.01	3.48±0.08	0.80±0.06	4.72±0.08	4.07±0.02
PLCK G100.5-30.4	4.7	23:22:14.9	28:31:13.5	0.31	0.40 <sup>(a)</sup>	0	0.76±0.01	4.7	1128	9.0±0.30	0.53±0.02	4.76±0.29	0.45±0.14	5.63±0.22	3.36±0.08
PLCK G308.5-20.2	8.3	...	...	...	...	2	1.0±0.01	3.9	1250	9.5±0.56	1.31±0.04	12.55±0.92	...	9.32±0.38	15.65±0.19
A	...	15:18:55.5	Ŝ81:30:30.1	0.48	...	...	...	...	...	...	...	...	...	...	...
B	...	15:16:52.6	Ŝ81:35:50.0	0.48	...	Ŝ1	0.42±0.01	2.9	894	3.7±0.35	0.55±0.03	2.09±0.25	...	3.41±0.23	8.67±0.26
PLCK G337.5-26.0	6.6	...	...	...	...	...	...	...	...	...	...	...	...	...	...
A	...	19:14:37.7	Ŝ59:28:16.7	0.26	...	2	3.2±0.03	7.5	1177	6.1±0.23	0.86±0.01	5.30±0.25	...	6.05±0.16	8.95±0.07
b	...	19:13:51.4	Ŝ59:33:51.6	0.12	...	2	1.7±0.02	4.5	749	2.8±0.20	0.12±0.01	0.34±0.03	...	1.34±0.07	1.02±0.01
PLCK G214.0-36.9	3.6	...	...	...	...	...	...	...	...	...	...	...	...	...	...
A	...	09:08:49.5	14:38:29.4	0.45	0.45	2	0.38±0.01	4.3	767	3.4±0.26	0.25±0.01	0.85±0.09	...	2.0±0.12	3.03±0.07
B	...	09:09:02.1	14:39:41.7	0.45	0.46	1	0.11±0.01	2.3	750	4.1±0.75	0.18±0.01	0.76±0.18	...	1.94±0.26	1.03±0.06
C	...	09:08:51.4	14:45:55.3	0.45	0.45 <sup>(a)</sup>	Ŝ1	0.25±0.01	3.1	809	3.7±0.50	0.30±0.01	1.13±0.19	...	2.44±0.23	2.28±0.08
PLCK G334.5-38.0	3.4	...	...	...	...	...	...	...	...	...	...	...	...	...	...
A	...	20:52:16.8	Ŝ61:12:29.4	0.35	...	2	0.13±0.01	1.8	722	3.1±0.33	0.15±0.01	0.48±0.07	...	1.55±0.13	0.77±0.06
B	...	20:53:08.0	Ŝ61:10:35.3	0.35	...	Ŝ1	0.08±0.01	3.2	605	2.0±0.31	0.09±0.01	0.19±0.05	...	0.91±0.12	0.47±0.33
C	...	20:52:44.3	Ŝ61:17:24.5	0.35	...	Ŝ1	0.03±0.00	1.2	607	3.1±1.71	0.06±0.02	0.19±0.18	...	0.92±0.44	0.21±0.06

Notes. Column (2): signal-to-noise ratio derived from the 10-mo Planck maps on the basis of which the ESZ sample was constructed. Columns (3)–(8): right ascension and declination of the peak of the X-ray image (2000). Column (9): redshift from X-ray spectral fitting. Column (10): optical redshift. Column (11): Quality flag for the X-ray redshift measurement (see Appendix A). Column (12): total count rates in the [0.3–2] keV band, within the maximum radius of detection given in Col. (13). Columns (14)–(16): the radius corresponding to a density contrast of 500, estimated iteratively from the  $M_{500}-Y_X$  relation (Eq. (1)), where  $Y_X = M_{500} T_X$  is the product of the gas mass with  $R_{500}$  and the spectroscopic temperature  $T_X$ , and  $M_{500}$  is the total mass within  $R_{500}$ .  $L_{500}$  is the luminosity in the [0.3–2.4] keV band and in the  $R_{500}$  aperture.  $Y_{500}$  is the spherically integrated Compton parameter measured with  $R_{500}$  centred on the X-ray peak, interior  $R_{500}$  as estimated with XMM-Newton (a) Photometric redshift. See Appendix A. (b) Photometric redshift for ACT-CL J0438-5419 Menanteau et al. (2010). (c) Rounded from 5.99 to 6.0, therefore not included in ESZ Planck Collaboration 2011. (d) Spectroscopic redshift. Redshift constrained from Fe L complex. Redshift assumed to be identical to that of component.

cases, the offset remains smaller than  $R_{500}$  or the cluster extent 6. X-ray and SZ properties of newly detected clusters (see also Fig 3).

## 5.2. Planck redefined $Y_{SZ}$ estimate

The SZ signal extraction procedure is described in detail in Planck Collaboration (2011d). It consists of applying multi-frequency matched filters to the data that maximally enhance the signal-to-noise ratio of an SZ cluster source by optimally filtering the data. As shown in Planck Collaboration (2011d), SZ fluxes derived using this method can be significantly overestimated due to an over-estimation of the cluster size.

We can optimise the SZ photometry of the clusters presented here by using the X-ray estimate of the cluster position and size, derived from  $R_{500}$  measured using the  $M_{500}-Y_X$  relation as detailed in Sect 5.1. For each cluster in the sample, we thus re-extract the SZ flux, calculating  $Y_{500}$  with the X-ray position and size fixed to the redefined values derived from the high-quality XMM-Newton observation. The resulting  $Y_{500}$  values are listed in Table 2. In Fig. 7, they are compared to the blind values as a function of the ratio of the XMM-Newton and blind characteristic size  $R_d$  to  $R_{500}$ . For most cases the values are consistent within the 1- $\sigma$  errors; however, there is a clear trend of SZ flux overestimation with size overestimation, which can reach as much as a factor of two (see detailed discussion of the cluster size-flux relation in Planck Collaboration 2011a and Planck Collaboration 2011g).

In this Section we consider the 17 systems confirmed as single-component clusters of galaxies, leaving aside the multiple systems which are discussed in the next section.

## 6.1. RASS properties

We extracted  $2 \times 2$  count images in the [6–22] keV hard band from the RASS data at the position of each cluster. We excluded events associated with known RASS-BSC and RASS-FSC sources (Voges et al. 1999, 2000). We then carefully followed the methods described in Böhringer et al. (2000) and Reiprich & Böhringer (2002) to compute background corrected growth curves and estimate an assumed detection radius  $R_d$ . The background was estimated from an outer annulus with  $45^\circ < \theta < 90^\circ$ . When allowed by the quality of the growth curve, the count rate within the  $R_{500}$  aperture was either taken as the count rate within the  $R_d$  when  $R_d < R_{500}$  or interpolated on the curve when  $R_d > R_{500}$ . Assuming the best fitting XMM-Newton spectral parameters for each cluster (i.e., temperature, abundance, galactic  $N_{\text{H}}$ ) we derived the [01–24] keV band RASS flux.

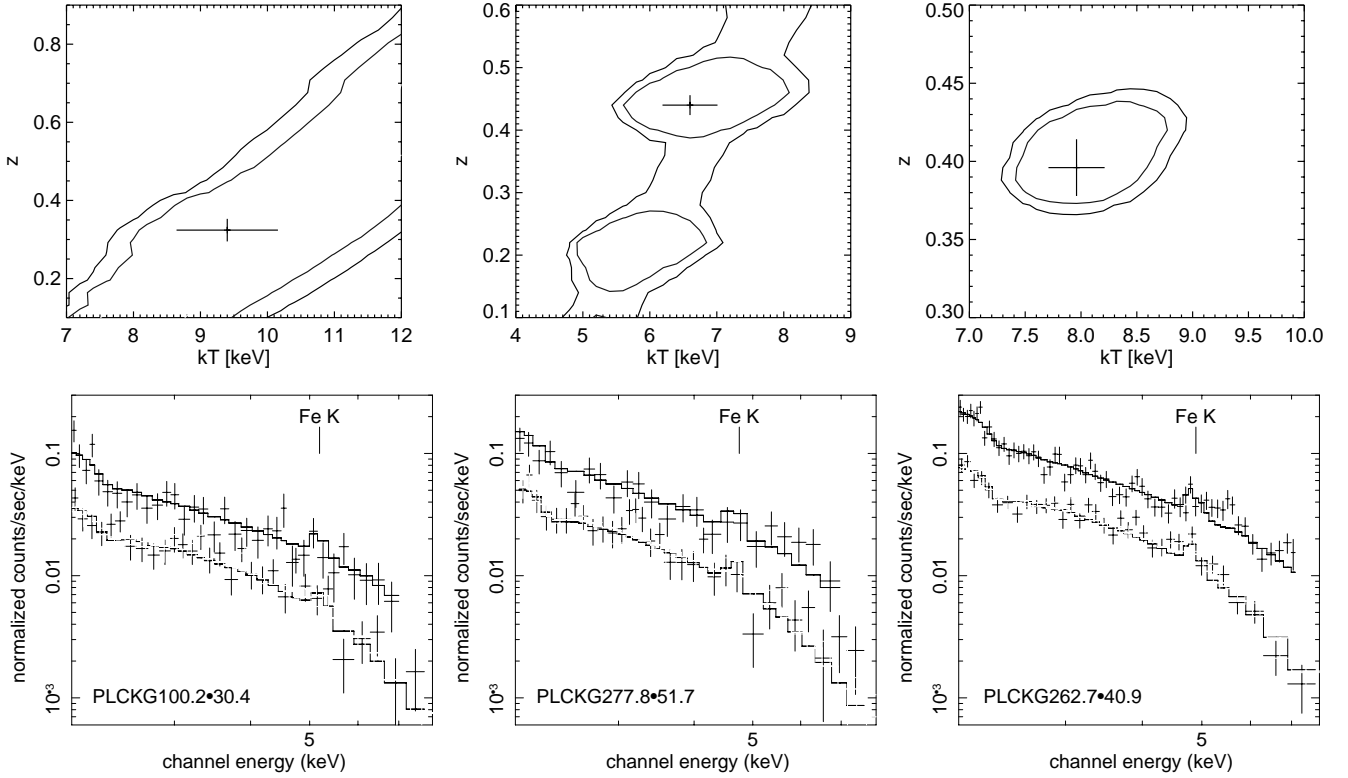


Fig. 5. Top row redshift determination from XMM-Newton spectroscopy in the  $kT$ - $z$  plane. Red, green and blue contours trace 68, 95 and 99.9 per cent confidence levels, respectively. The black error point shows the best-fitting spectral results with associated statistical errors. Bottom row shows the corresponding X-ray spectra (red and black points) and (green points) spectra. Only the data points above 2 keV are shown for clarity but data down to 0.3 keV are used in the spectral fitting. The line is the thermal model for the best-fitting redshift. The position of the redshifted Fe K line is marked. From left to right the figures are for sources PLCK G100.2+30.4, PLCK G277.8+51.7 and PLCK G241.2+28.7.

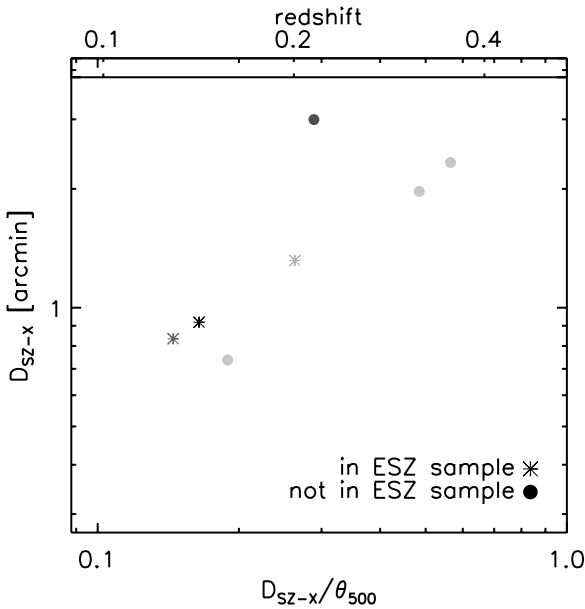


Fig. 6. Distance of blind SZ position to X-ray position  $D_{SZ-X}$ , as a function of  $D_{SZ-X}$ , normalised to the cluster size  $\theta_{500}$  for single confirmed systems. The clusters are colour-coded according to redshift. Note that the offset is typically less than 2" and always less than  $3\theta_{500}$ .

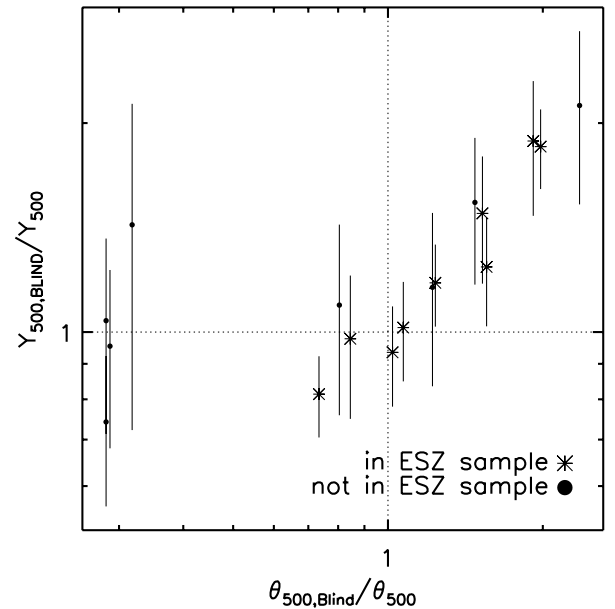


Fig. 7. Comparison of the Planck blind and X-ray constrained  $Y_{500}$  measurements for single confirmed systems (see text, Sect. 3.2). The ratio is not correlated with the ratio of the corresponding characteristic size,  $\theta_{500}$ .

The RASS values are compared to XMM-Newton values in Fig. 8. There is a good agreement after taking into account the RASS statistical errors. The slight offset ( $<20\%$ ) is likely due to systematic errors linked to the RASS background

estimate and/or calibration uncertainties. The most significant outlier at high flux is PLCK G18.7+23.6. A bright point source is present at the centre of this object (see Fig. 3) that cannot be excised from the RASS data and which contaminates the signal. From the XMM-Newton image (Fig. 3), the known

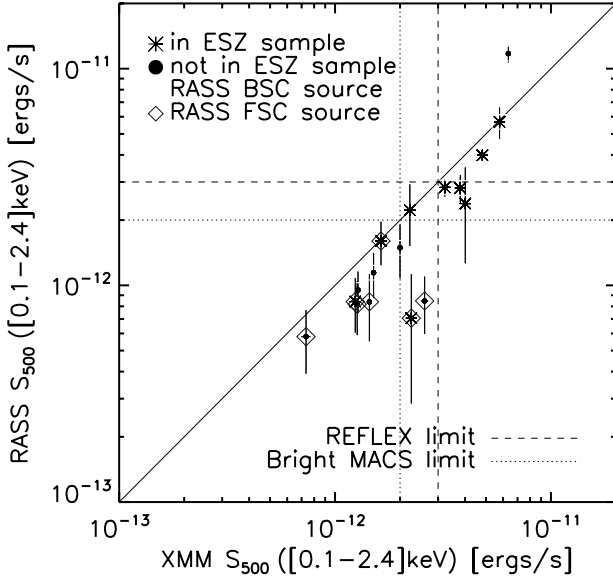


Fig. 8. Unabsorbed RASS  $u_{500}$  versus XMM-Newton  $u_{500}$  for the 17 confirmed single-component clusters. The  $[0.1–2.4]$  keV  $u_{500}$  is measured within an aperture of  $500''$ . Clusters coincident with a RASS-BSC or a RASS-FSC source are marked with red squares and green diamonds, respectively. The most significant outlier at high  $u_{500}$  is PLCK G18.7-23.6 at  $z = 0.09$  (see Sects. 6.1 and 6.2 for discussion).

RASS-FSC or RASS-BSC sources within the Planck error box for 15 of the candidates can be clearly identified with the clusters. Those are indicated in Fig. 8. The two clusters with no RASS-FSC or RASS-BSC association, PLCK G287.0-9 and PLCK G292.5-22.0, are in fact detected in RASS, but at low S/N (2 and 3, respectively; see also Sect. 6.4).

## 6.2. The $L_{X,SZ}$ plane and comparison with RASS catalogues

In Fig. 9, the new clusters are shown in the  $u_{500}$ - $z$  plane, plotted together with the clusters from large catalogues based on RASS data outside the Galactic Plane: REFLEX (Böhringer et al. 2004) in the Southern sky; NORAS (Böhringer et al. 2000) BCS (Ebeling et al. 1998) and eBCS (Ebeling et al. 2000) in the Northern Sky. The NORAS is not  $u_{500}$  limited. The REFLEX  $u_{500}$  limit of  $3 \times 10^{512} \text{ erg s}^{-1} \text{ cm}^{-2}$  is shown. It is similar to that of the eBCS-BCS limit of  $2.8 \times 10^{512} \text{ erg s}^{-1} \text{ cm}^{-2}$ . Also shown are clusters from the published catalogues of the MACS survey with their corresponding  $u_{500}$  limit. MACS is based on the RASS-BSC but in contrast to the above surveys, the X-ray extent of the RASS source is not a selection criterion, allowing more distant (but massive) clusters to be found (Ebeling et al. 2001). Published MACS catalogues are the 0.5 catalogue (Ebeling et al. 2007) and the  $0.3 < z < 0.5$  brightest cluster catalogue (Ebeling et al. 2007, hereafter bright MACS). Luminosities plotted in Fig. 9 are the homogenised values given in the MCXC (Meta-Catalogue of X-ray detected Clusters of galaxies; Piarotti et al. 2011).

The present sample of new Planck-detected systems spans a redshift range of  $0 < z < 0.6$ , with 15 out of 17 clusters above  $z = 0.25$ , a medium-distant redshift region of the  $u_{500}$ - $z$  plane that is sparsely-populated by the RASS catalogues. As a consequence, our current sample has X-ray luminosities well below the  $u_{500}$  limit of HIFLUCGS (Reiprich & Böhringer 2002) and REFLEX-DXL (Zhang et al. 2006) two high-luminosity X-ray selected samples that stand as the counterparts to our present high S/N SZ sample. The closest sample in X-ray luminosity

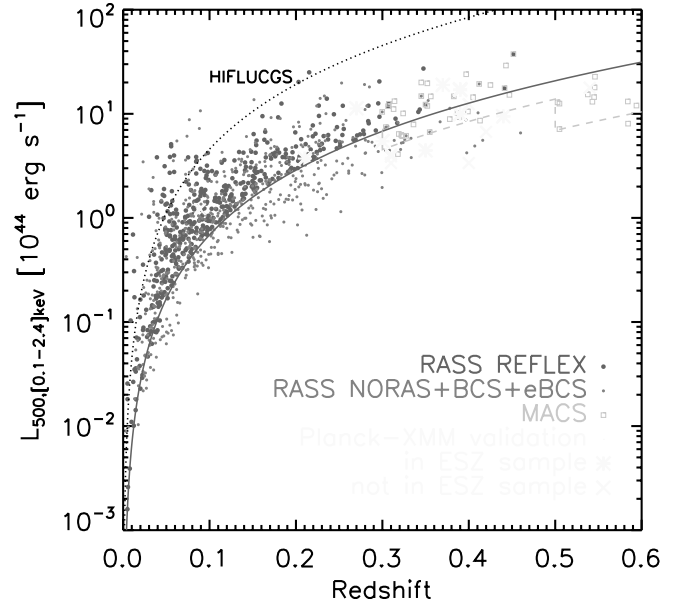


Fig. 9. The new SZ-discovered Planck clusters compared to clusters from the ROSAT All-Sky Survey catalogues in the  $u_{500}$ - $z$  plane. The X-ray luminosity is that in the  $[0.1–2.4]$  keV band. Catalogues shown are the REFLEX, NORAS, BCS, eBCS and published MACS catalogues. The solid line is the REFLEX  $u_{500}$  limit of  $3 \times 10^{512} \text{ erg s}^{-1} \text{ cm}^{-2}$ , similar to that of the BCS-eBCS catalogues. The dotted line is the HIFLUCGS  $u_{500}$  limit of  $2 \times 10^{511} \text{ erg s}^{-1} \text{ cm}^{-2}$  and the dashed line is from the MACS  $u_{500}$  limits. See Sect. 6.2 for references and details.

and redshift to the new Planck clusters are the MACS clusters, although the Planck clusters go to lower luminosity.

Most of the new Planck clusters naturally fall below the REFLEX  $u_{500}$  limit or, equivalently, the BCS-eBCS limit in the North. However, three clusters lie well above this limit: PLCK G18.7-23.6, PLCK G171.9-40.7, PLCK G271.3-31.0, in order of decreasing X-ray  $u_{500}$  (Fig. 8 and 9). As discussed above, PLCK G18.7-23.6 at  $z = 0.09$  has a very bright central source and very diffuse ICM emission. It may have been misclassified as a point source in the REFLEX survey. We also note that this cluster, although not included in the ESZ sample, is the brightest X-ray cluster of the sample due to its low redshift  $z = 0.09$ . PLCK G271.3-31.0 simply falls in the Large Magellanic Cloud LMC2 region, which was excluded in the REFLEX survey (see Böhringer et al. 2001, Table 1). However, PLCK G171.9-40.7 at  $z = 0.27$  has a  $u_{500}$  of  $57 \times 10^{512} \text{ erg s}^{-1} \text{ cm}^{-2}$  (from fully consistent ROSAT and XMM-Newton measurements), and is a northern sky cluster that fulfills the BCS  $u_{500}$  and sky position criteria. Thus a priori, it should have been included in that survey. Finally, six new clusters at  $z > 0.3$  are above the MACS  $u_{500}$  limit. Of these, four are not associated with a RASS-BSC source and so could not be found in a MACS-like survey, and the other two are at lower declination than considered by MACS.

## 6.3. Gas morphology and scaled density profiles

Figure 3 shows  $[0.3–2]$  keV XMM-Newton images of the newly-discovered clusters. Each image corresponds to the same physical size in units of  $R_{500}$  and is corrected for surface brightness dimming with redshift and divided by the emissivity in the  $[0.3–2]$  keV energy band. As detailed in Arnaud et al. (2002, Sect. 3.2), the emissivity is computed from a redshifted thermal profile convolved with the instrument response and taking into account Galactic absorption. The resulting image is proportional

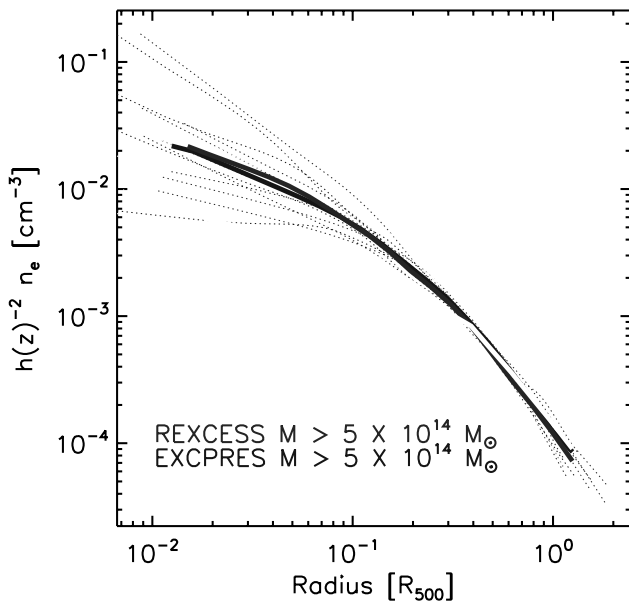


Fig. 10. Scaled density profiles of the new Planck SZ clusters compared to those of similar mass systems from the representative X-ray samples REXCESS (Böhringer et al. 2007) and EXCPRES (Arnaud et al., in prep.).  $R_{500}$  is estimated from the  $M_{500}-Y_X$  relation of Arnaud et al. (2010). Thick lines show the mean profile of each sample. The density profiles of the Planck SZ-selected clusters are on average shallower than those of the X-ray selected clusters of the same mass.

to the emission measure along the line of sight, which is then scaled by  $E(z)^2 R_{500}$  according to the self-similar model. The colour table is the same for all clusters, so that the images would be identical if clusters obeyed strict self-similarity. A first visual impression is that low surface brightness, morphologically disturbed objects dominate the sample, which contains very few centrally-peaked, cool core-like objects.

The visual impression is confirmed and quantified when one looks at the density profiles of the clusters shown in Fig. 10. They are plotted together with the density profiles of similar mass clusters from the representative X-ray-selected samples REXCESS ( $z < 0.2$ ; Böhringer et al. 2007) and EXCPRES ( $0.4 < z < 0.6$ ; Arnaud et al., in prep.). For all three samples, the radii are scaled by  $R_{500}$ , estimated from the  $M_{500}-Y_X$  relation (Eq. (1)). The thick lines show the mean profile. While the two X-ray-selected samples agree to a remarkable degree, the Planck-selected sample clearly consists of systems with much flatter density profiles, and the corresponding mean profile is significantly flatter than that of the X-ray selected samples. This shape is due to a number of very disturbed clusters with very flat profiles in the new Planck-discovered cluster sample. Let us consider the ten clusters with the flattest density profiles, flatter than the mean profile of the Planck cluster sample and flatter than all the REXCESS profiles. These ten objects include PLCK G18.7-23.6 at  $z = 0.09$  discussed above, PLCK G286.6-31.3 at  $z = 0.21$  that is just at the REFLEX flux limit and PLCK G292.5+22.0 at  $z = 0.30$  that is just at the MACS flux limit (Fig. 9). The other seven clusters lie at medium redshift,  $0.3 < z < 0.45$ , and are all hot ( $T_X > 5$  keV) and massive ( $M_{500} > 5 \times 10^{14} M_\odot$ ) systems. They lie below the flux limit of both REFLEX and bright MACS for a similar mass range (Ebeling et al. 2010). Thus Planck appears to have uncovered a population of massive, disturbed, low-luminosity systems.

#### 6.4. SZ flux versus X-ray prediction and mass-proxy $D$ mass relations

Planck Collaboration (2011g) uses XMM-Newton archival data to study the relations between the SZ signal and X-ray properties such as  $Y_X$  or the soft band luminosity  $L_{500}$  on a sub-sample of clusters from the high signal-to-noise ratio ESZ sample. This sample (hereafter the ESZMM-archive sample) is SZ selected but by nature only comprises clusters from X-ray surveys. As discussed extensively in Planck Collaboration (2011g), the analysis has demonstrated the excellent agreement between the observed scaling relations and the predictions based on X-ray pressure profiles and numerical simulations (Arnaud et al. 2010). In Fig. 11, we have placed the new Planck XMM-Newton confirmed clusters on the  $Y_{500}-Y_X$  relations (top panels) and the  $L_{500}-Y_{500}$  and  $M_{500}-L_{500}$  relations (bottom panels).

##### 6.4.1. The $Y_{500}-Y_X$ relation

The SZ signal,  $Y_{500}$ , is plotted as a function of the normalized  $D_A^2 Y_X$  parameter in the left panel of Fig. 1. The new clusters follow the trend observed for the ESZMM-archive and are consistent with the EXCESS prediction (blue line). However, a slight turnover is observed at low  $Y_X$ , with observed points systematically above the predicted relation. This excess is likely due to the Malmquist bias. Such a trend is also slightly apparent for the ESZMM-archive sample but is less important (see Planck Collaboration 2011g for discussion of this effect). The low  $Y_X$  clusters span various values and are redistributed over the range of intrinsic Compton parameter. As a result there is a slight positive offset apparent in the  $D_A^2 Y_{500}-Y_X$  relation for new clusters as compared to the ESZMM-archive sample.

This suggests that as far as the relation between  $Y_{500}$  and its X-ray equivalent  $Y_X$  is concerned, the new clusters are similar to X-ray selected clusters, although they are more dynamically disturbed. This is expected if indeed the pressure is the quantity less affected by dynamical state and both  $Y_X$  and  $Y_{500}$  are low scatter mass proxies. However, independent mass estimates are required to check this point; they cannot be provided by X-ray measurements in view of the highly unrelaxed nature of the new clusters.

##### 6.4.2. The $L_{500}-Y_{500}$ and $M_{500}-L_{500}$ relations

As compared to X-ray selected clusters, the new clusters fall on the low luminosity side of the  $L_{500}-Y_{500}$  relation (bottom left panel of Fig. 11). In other words, they are under-luminous at given  $Y_{500}$ . If the mass is indeed tightly related to  $Y_{500}$  (or  $Y_X$ ) we then expect them to be under-luminous at a given mass. This trend is consistently observed in the bottom-right panel, where  $M_{500}$  is estimated from  $Y_X$ : the new clusters fall towards the high-mass, low-luminosity side of the  $M_{500}-L_{500}$  relation. However, confirmation requires independent mass estimates, e.g., from lensing data.

As shown by Pratt et al. (2009), the underluminous region of the  $L-M$  plane is populated by morphologically disturbed systems. This once again suggests that the majority of the new Planck-detected systems are disturbed, in agreement with the above discussion on the morphology and the scaled density profiles.

The dispersion of the new clusters about the  $M_{500}-L_{500}$  relation also seems higher than that for X-ray selected objects. This suggests the existence of new extreme low-luminosity, high-mass objects that are being revealed by Planck. The two prominent outliers are PLCK G287.0-32.9 ( $z = 0.39$ ) and

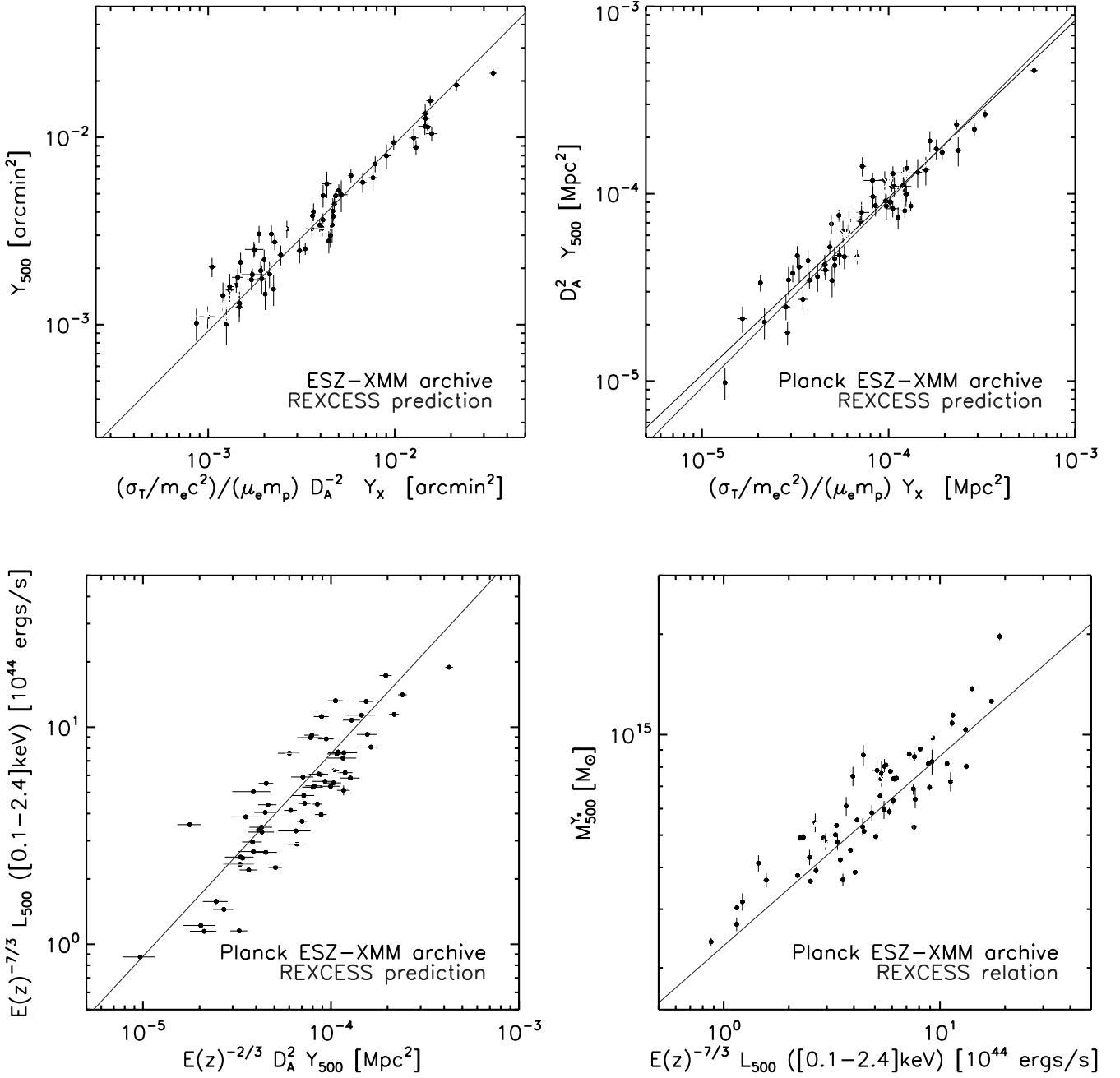


Fig. 11. Scaling relations for the 17 new confirmed single-component clusters (red symbols). Black points show clusters in the Planck ESZ sample with XMM-Newton archival data as presented in Planck Collaboration (2011g). The solid black line denotes the corresponding scaling relation in each panel. The blue lines in the top and bottom right panels denote the predicted  $Y_{500}$  scaling relations from the REXCESS X-ray observations (Arnaud et al. 2010). The blue line in the bottom left panel is the Malmquist bias corrected  $M-L$  relation from the REXCESS sample (Pratt et al. 2009, Arnaud et al. 2010). In all figures  $R_{500}$  and  $M_{500}$  are estimated from the  $M_{500}-Y_X$  relation of Arnaud et al. (2010). Top row relation between apparent SZ signal ( $Y_{500}$ , left) or intrinsic Compton parameter ( $D_A^2 Y_{500}$ , right) and the corresponding normalized Compton parameter. Bottom row relation between X-ray luminosity and  $Y_{500}$  (left) and between mass and luminosity (right panel). The new clusters are on average less luminous at a given  $Y_{500}$ , or more massive at a given luminosity, than X-ray selected clusters.

PLCK G292.5+22.0 ( $z = 0.3$ ), detected by Planck at high SN values of 10.6 and 6.9, respectively. They belong to the very hot ( $T > 10$  keV) and very massive ( $M_{500} > 10^{15} M_\odot$ ) cluster category (Table 2) and are the only two clusters associated with neither a BSC nor an FSC source (Sect. 6.1 and Fig. 8).

The flux of PLCK G292.5+22.0 barely reaches the MACS limit for a mass of  $M_{500} = 9.2 \times 10^{14} M_\odot$ . It has a very disturbed morphology (Fig. 3) and a flat density profile with a scaled central density of  $4 \times 10^{-23} \text{ cm}^{-3}$  (Fig. 10).

7. Further analysis of multiple systems

#### 7.1. Double systems

Two of the new Planck sources (PLCK G308.3+20.2 and PLCK G337.5+26.0) were revealed by the XMM-Newton validation observations to be double systems. X-ray images of these systems are included in the gallery in Fig. 9.

